Taylor Couette Instability in Disk Suspensions: Experimental Observation and Theory

J. J. J. Gillissen[1], N. Cagney[2,3], T. Lacassagne[3], A. Papadopoulou[3], S. Balabani[3] and H. J. Wilson[1]
[1] *Department of Mathematics, University College London, Gower Street, London WC1E 6BT, United Kingdom*
[2] *School of Engineering and Materials Science, Queen Mary University of London, United Kingdom*
[3] *Department of Mechanical Engineering, University College London, United Kingdom**
(Dated: January 21, 2020)

We report on a new type of Taylor Couette instability, that is neither driven by inertia nor by elasticity. Instead the instability is driven by anisotropic viscous stresses induced by suspended disk-shaped particles, that redirect azimuthal momentum transfer from the radial to the axial direction. We provide experimental evidence for the instability, using suspensions of mica flakes, which act as flow destabilisers and also as flow visualisers. As a function of the mica concentration, there is good agreement between theory of dilute disk suspensions and experiment in the concentration dependence of the critical speed for instability onset and of the axial wavelength of the corresponding instability mode.

PACS numbers:

Taylor Couette flow (TCF) is the flow in the gap between two counter rotating cylinders. When the outer cylinder is held fixed, and the rotation speed of the inner cylinder exceeds a threshold value, the circular Taylor Couette base flow destabilises, which is accompanied by the emergence of so-called Taylor vortices [1]. For Newtonian fluids, the onset of instability corresponds to the Taylor number $\mathrm{Ta} = \rho\Omega\sqrt{\Delta R^3 R_1}/\eta_s$, exceeding a critical value Ta_c, that, depending on the cylinder radius ratio R_2/R_1, is around $\mathrm{Ta}_c \approx 50$. Here η_s is the fluid viscosity, Ω is the angular velocity of the inner cylinder, $\Delta R = R_2 - R_1$ is the gap width between the cylinders, and R_1 and R_2 are the radii of the inner and of the outer cylinder, respectively.

In non-Newtonian fluids the behaviour is different, and to date two types of non-Newtonian TCF instabilities have been observed. The first type is driven by centrifugal forces, similar to the Newtonian instability, described above. In this case the non-Newtonian rheology only alters the details of the instability, i.e. the onset speed, the shape and the dynamics of the vortical structures, while the driving force remains the same. Examples of this type of instability include fluids with a shear thinning rheology [2–4] or suspensions of rod-like polymers, e.g. polyacrylic acid, xanthan and carboxymethyl cellulose [5–8]. Other examples include dense suspensions of spheres [9–11], where non-Newtonian effects arise from an anisotropic microstructure as well as from slippage between the fluid and solid phases [9, 12].

The second type of non-Newtonian TCF instability is driven by viscoelastic stresses and persists even in the absence of centrifugal forces. This so-called "elastic instability" has been observed in polymer solutions: [13–15] and in micelle solutions [16] where in the later case, the instability is also affected by shear banding, i.e. by a non-monotonic relationship between the stress and the strain rate. The elastic instability is well understood and reproduced by numerical simulation using constitutive equations of viscoelastic fluids [14, 17].

In this work we report on a third type of TCF instability, that is neither driven by inertia nor by elasticity. This instability is driven by the anisotropic viscous stresses in suspensions of disk-shaped particles, which redirect azimuthal momentum transfer from the radial to the axial direction. Theory predicts that for infinite disk aspect ratio and for vanishing rotary diffusion, the instability persists for vanishing flow inertia, albeit with a vanishing instability growth rate. Rotary diffusion and finite aspect ratio both have an adverse effect on the instability, requiring a finite flow speed for instability onset [8].

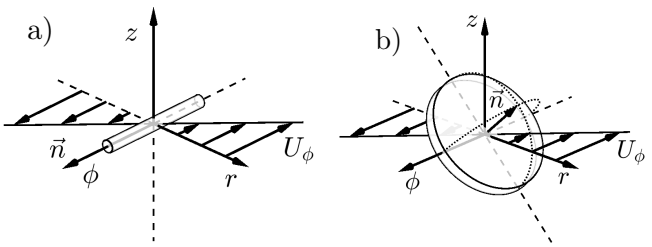

FIG. 1: (a) A rod with its major axis $\boldsymbol{n}$ in the azimuthal direction ϕ, does not rotate when subjected to an azimuthal vorticity perturbation. (b) A disk on the other hand tilts its normal $\boldsymbol{n}$ away from the radial direction r towards the axial direction z. The mean flow field $U_\phi(r)$ is drawn relative to the motion of the particles.

We explain the destabilising effect of suspended disks, by contrasting it to the negligible effect of suspended rods. Fig. 1a illustrates a rod in the Taylor Couette base flow which has a strain rate $s_{\phi r}$. The flow, gradient and

*Electronic address: jurriaangillissen@gmail.com

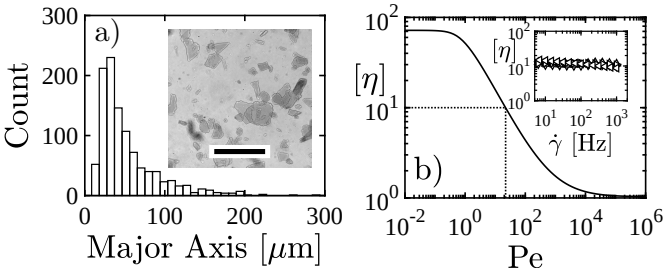

FIG. 2: (a) Mica size distribution, obtained from micrographs, as shown in the inset which has a 200 μm scale bar. (b) The theoretical, intrinsic viscosity $[\eta]$ as a function of the rotary Peclet number Pe in dilute suspensions of disks with an aspect ratio of $r_a^{-1} = 10^2$. The dotted lines indicate the rotary Peclet value Pe ≈ 22 that corresponds to the measured $[\eta] \approx 10$. The inset shows the experimentally measured intrinsic viscosity in mica suspensions as a function of the shear rate, for $c = 5 \times 10^{-3}$ (downward triangle), $c = 10^{-2}$ (upward triangle), $c = 2 \times 10^{-2}$ (rightward triangle) and $c = 5 \times 10^{-2}$ (leftward triangle).

vorticity directions are ϕ, r and z, respectively. In the limit of an infinite aspect ratio and zero rotary diffusion, the rod major axis $\boldsymbol{n}$ points in the ϕ-direction and generates no additional stress. A Taylor vortex perturbation corresponds to azimuthal fluid vorticity ω'_ϕ, i.e. to fluid rotation around $\boldsymbol{n}$. Consequently $\boldsymbol{n}$ remains fixed and the rod generates no hydrodynamic stress.

For a disk, the situation is sketched in Fig. 1b. In the base flow, the disk normal $\boldsymbol{n}$ points in the r-direction. A Taylor vortex perturbation ω'_ϕ rotates $\boldsymbol{n}$ away from the r-axis and towards the z-axis. The perturbation of the disk normal in the z-direction n'_z generates a stress perturbation $\sigma'_{\phi z} \sim s_{\phi r} n_r n'_z$ [Eq. (3) below]. This stress perturbation has an amplifying feedback on the Taylor vortex perturbation ω'_ϕ via $\partial_t u'_\phi \sim \partial_z \sigma'_{\phi z}$ and $\partial_t u'_r \sim (U/R) u'_\phi$ [Eq. (2) below] and $\omega'_\phi \sim \partial_z u'_r$.

The TCF instability in dilute disk suspensions is driven by anisotropic viscous stresses and in theory the instability persists in the absence of inertial stresses, elastic stresses and shear thinning effects [8]. A related but not entirely similar instability has been observed in suspensions of disk-shaped clay particles [18]. These clay suspensions however generate elastic stresses and shear thinning due to rotary diffusion and electrostatic interparticle forces [19]. These effects destabilise TCF even in the absence of anisotropic viscous stresses [2].

In this work we provide experimental evidence for the TCF instability in dilute suspensions of non-Brownian and (nearly) non-adhesive disks. To this end we use suspensions of mica flakes (Cornellius Ltd.) with a thickness of $d \approx 1$ μm and a mass density of 2.93 g cm^{-3}. In addition to inducing hydrodynamic instability, the mica flakes also serve to visualise the flow. Fig. 2a shows the distribution of the major particle axis l which is obtained from 20 micrographs, as shown in the inset of Fig. 2a.

We examine one Newtonian fluid, i.e. with a very low disk concentration $c = 10^{-4}$, and five disk suspensions with volume fractions ranging between $c = 10^{-3}$ and $c = 5 \times 10^{-2}$. The suspending medium is a mixture of glycerol (volume fraction G), distilled water (volume fraction W) and aqueous food dye to aid flow visualisation (volume fraction 0.02). For $c \leq 10^{-2}$ and $c \geq 2 \times 10^{-2}$ we used (G,W) = (0.71, 0.27) and (0.9, 0.08) respectively, which correspond to a density and a viscosity of (ρ [g cm^{-3}], η_s [Pa s]) of (1.18, 0.036) and (1.24, 0.3), where the more viscous liquid was used to suppress sedimentation effects at the higher mica concentrations.

The steady shear viscosity η_{eff} of the suspensions is measured using a rotational rheometer (TA Instruments) equipped with a cone-and-plate geometry. The inset of Fig. 2b shows the measured intrinsic viscosity $[\eta] = (\eta_{\text{eff}} - \eta_s)/(c\eta_s)$, as a function of the shear rate $\dot{\gamma}$ for the various suspensions. The shear rate range $5 \leq \dot{\gamma} \leq 10^3$ Hz would correspond to a Taylor number range in the TCF setup of approximately $3 \leq \text{Ta} \leq 6 \times 10^2$. The measured $[\eta]$ collapse for the various c, i.e. $[\eta]$ is independent of c, causing overlapping and invisible markers in the inset of Fig. 2b. Moreover, for $c \leq 2 \times 10^{-2}$ we see that $[\eta]$ is independent of $\dot{\gamma}$, and for $c = 5 \times 10^{-2}$ there is a slight shear thinning $[\eta] \sim \dot{\gamma}^{-0.02}$. The suspensions are therefore (nearly) rate independent, which confirms absence of adhesion forces and the corresponding elastic behaviour.

The cylinders in the TCF setup have length $L = 155$ mm and radii $R_1 = 21.66$ mm and $R_2 = 27.92$ mm which correspond to a radius ratio of $R_1/R_2 = 0.77$ and an aspect ratio of $L/\Delta R = 21.56$. The flow cell is enclosed within a rectangular chamber in which water is recirculated, to keep the fluid temperature in the flow cell at 20 ± 0.1°C [4].

For $c \leq 2 \times 10^{-2}$ we accelerate the inner cylinder from rest with $\mathrm{d}\Omega/\mathrm{d}t = 0.16$ rad/s^2 to a maximum speed of 114 rad/s. To suppress sedimentation effects we also conducted runs where we decelerate from 114 rad/s with $\mathrm{d}\Omega/\mathrm{d}t = -0.16$ rad/s^2. All runs were repeated for both acceleration and deceleration, giving very similar results for critical speed and size of vortices. the non-dimensional acceleration rate: $\mathrm{d}\Omega^*/\mathrm{d}t^* = (\rho^2 R_1 \Delta R^3/\eta_{\text{eff}}^2)|\mathrm{d}\Omega/\mathrm{d}t| < 1$ to ensure a quasi-steady flow [20].

To observe the flow patterns, we illuminate the flow cell using a white light-emitting diode (SugarCUBE, Edmund Optics) and we image a strip of the flow cell with a CMOS camera (Phantom Miro 340) at a frame rate of 60 Hz and a resolution of 2224×16 pixels in the z and ϕ directions. Each image is averaged over ϕ into an axial profile with 2224 pixels and all profiles are combined into a matrix, or 'flow map', of the light intensity as a function of z and Ta [4].

The flow maps in Figs. 3a-b for $c = 10^{-4}$ and $c = 10^{-2}$ show that above a critical Ta the circular base flow transitions into a vortical flow, indicated by the appearance of intensity bands. Flow maps for the higher concentrations are provided in the Supplementary Information.

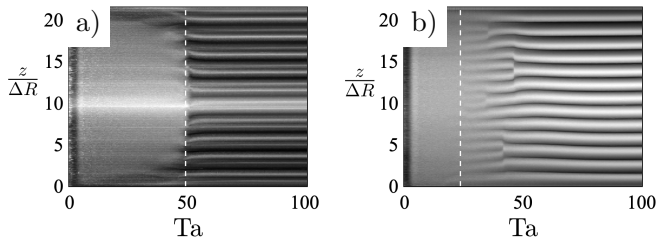

FIG. 3: Flow visualisation for mica suspensions with concentrations of $c = 10^{-4}$ (a) and $c = 10^{-2}$ (b). The intensity maps show the onset of instability as the appearance of the banded structures above a critical speed, indicated by the dashed white lines.

These bands are horizontal which shows that the vortices are axisymmetric and non-oscillatory. The onset of instability corresponds to critical values, k_c and Ta_c, of the axial vortical wavenumber k and of the effective Taylor number $\mathrm{Ta} = \rho\Omega\sqrt{\Delta R^3 R_1}/\eta_{\mathrm{eff}}$ which is based on the measured effective viscosity η_{eff} (inset of Fig. 2b). For the details of determining these critical values, we refer to the Supplementary Information.

In the suspension with negligible mica concentration $c = 10^{-4}$ (Fig. 3a), Ekman vortices develop at the ends of the flow cell before the instability sets in across the entire axial span, at $\mathrm{Ta}_c \approx 49$, which is very close to the theoretical value $\mathrm{Ta}_c \approx 48$ [21]. For $\mathrm{Ta} > \mathrm{Ta}_c$, there are no significant changes in the intensity map (Fig. 3a), suggesting that the magnitude of the instability mode does not depend strongly on Ta in this regime.

In the suspension with substantial mica concentration $c = 10^{-2}$ (Fig. 3b) faint ridges appear for $\mathrm{Ta} > \mathrm{Ta}_c \approx 24$, which gradually become more distinct as Ta is increased further. This indicates that at $\mathrm{Ta} = \mathrm{Ta}_c$ the vortex strength is weak relative to the Newtonian mode, and it grows for $\mathrm{Ta} > \mathrm{Ta}_c$. It is noted that this gradual development of the mode intensity is not observed in similar measurements of solutions of flexible or rod-like polymers [4].

The flow map for $c = 10^{-2}$ in Fig. 3b shows another interesting feature of the disk mode; as Ta is increased, the number of vortices (indicated by the number of bright and dark bands) abruptly decreases at several points, corresponding to sudden increases in the axial vortical wavelength. This phenomenon has also been observed in solutions of polymers [4, 22]. It is also noted that these jumps are due to the finite $L/\Delta R$ of the TCF setup, while for $L/\Delta R \to \infty$ these changes are continuous.

We now compare the experimental results to a theoretical model [8]. The model is based on the constitutive equations for dilute suspensions of spheroids which are given by the continuity equation [23]:

$$\boldsymbol{\nabla} \cdot \boldsymbol{u} = 0, \tag{1}$$

and the momentum equation:

$$\rho \partial_t \boldsymbol{u} = \boldsymbol{\nabla} \cdot \left(-\rho \boldsymbol{u}\boldsymbol{u} - p\boldsymbol{\delta} + \eta_s \left(\boldsymbol{\nabla}\boldsymbol{u} + \boldsymbol{\nabla}\boldsymbol{u}^T \right) + \boldsymbol{\sigma} \right), \tag{2}$$

where the spheroid stress $\boldsymbol{\sigma}$:

$$\frac{\boldsymbol{\sigma}}{\eta_s} = 2\alpha_1 \boldsymbol{s} + 2\alpha_2 \boldsymbol{s} : \boldsymbol{a}\boldsymbol{a} + \alpha_3 \left(\boldsymbol{s} \cdot \boldsymbol{a} + \boldsymbol{a} \cdot \boldsymbol{s} \right) + \alpha_4 D_r \left(\boldsymbol{a} - \tfrac{1}{3}\boldsymbol{\delta} \right), \tag{3}$$

depends on the microstructure $\boldsymbol{a} = \langle \boldsymbol{n}\boldsymbol{n} \rangle$ where $\boldsymbol{n}$ is the unit vector along the spheroid polar axis and $\langle \cdots \rangle$ is the average that is weighted with the probability density function of $\boldsymbol{n}$. The microstructure tensor $\boldsymbol{a}$ evolves as:

$$\partial_t \boldsymbol{a} = -\boldsymbol{u} \cdot \boldsymbol{\nabla}\boldsymbol{a} + \boldsymbol{\nabla}\boldsymbol{u}^T \cdot \boldsymbol{a} + \boldsymbol{a} \cdot \boldsymbol{\nabla}\boldsymbol{u} + (B-1)\left(\boldsymbol{s} \cdot \boldsymbol{a} + \boldsymbol{a} \cdot \boldsymbol{s} \right) - 2B\boldsymbol{s} : \boldsymbol{a}\boldsymbol{a} - D_r \left(\boldsymbol{a} - \tfrac{1}{3}\boldsymbol{\delta} \right). \tag{4}$$

Here $\boldsymbol{u}$ is the velocity, ρ is the suspension mass density, p is the pressure, $\boldsymbol{s} = \frac{1}{2}\left(\boldsymbol{\nabla}\boldsymbol{u} + \boldsymbol{\nabla}\boldsymbol{u}^T \right)$ is the rate of strain tensor, $D_r \sim k_B T/(\eta_s d^3)$ is the rotary diffusivity which is added to mimic the effects of hydrodynamic interactions between the non-Brownian disks, c is the spheroid volume fraction, $r_a = a/b$ is the aspect ratio, a is the polar radius b is the equatorial radius, α_i are material constants that depend on c and r_a and $B = (r_a^2 - 1)/(r_a^2 + 1)$. The cases: $r_a < 1$, $r_a = 1$ and $r_a > 1$ correspond to oblate spheroids (disks), spheres and prolate spheroids (rods), respectively.

In order to estimate the effective aspect ratio that corresponds to the size distribution in Fig. 2a, we use that the disk stress $\boldsymbol{\sigma}$ scales with the disk major axis cubed [23]. Therefore the relevant particle dimension is the cube root of the third moment of this distribution $l_{\mathrm{eff}} = \langle l^3 \rangle^{1/3} \sim 10^2$ μm, giving an aspect ratio of $r_a^{-1} = l_{\mathrm{eff}}/d \sim 10^2$.

In the dilute theory [Eqs. (1-4)] hydrodynamic interactions are not taken into account rigorously. The number of these interactions per particle is proportional to the volume fraction of the disk-circumscribing spheres $\sim c r_a^{-1}$. In the present work, we consider mica suspensions with concentrations up to $c r_a^{-1} \sim 5$, for which hydrodynamic interactions are expected to be important. We model these effects with the rotary diffusion terms (D_r terms) in Eqs. (3-4). Theoretical and experimental studies have shown that rotary diffusion is an adequate model for hydrodynamic interactions between rods [24–28]. For disks on the other hand there are no equivalent studies and at present it is not clear if interactions can adequately be modelled by rotary diffusion. Below, we shed some light on this issue by comparing the theoretical model [Eqs. (1-4)] to experimental data, for both steady shear flow and for the TCF instability.

First we show in Fig. 2b the theoretical [Eqs. (1-4)] intrinsic viscosity $[\eta]$ in the steady shear flow of a suspension of oblate spheroids with an aspect ratio of $r_a^{-1} = 10^2$ as a function of the rotary Peclet number $\mathrm{Pe} = \dot{\gamma}/D_r$. The theoretical viscosity in Fig. 2b decreases as a function of Pe. For $\mathrm{Pe} \approx 22$ the model matches the experimental data $[\eta] \approx 10$ (inset of Fig. 2b). We reemphasize that the mica flakes are non-Brownian and that rotary

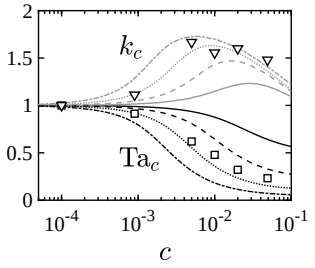

FIG. 4: The critical Taylor number Ta_c (black lines and squares) and the critical vortical wavenumber k_c (grey lines and triangles), normalised by their Newtonian values, plotted versus the disk concentration c. Comparison between experimental data (markers) and theory (lines) . The theory uses an aspect ratio of $r_a^{-1} = 10^2$ and a rotary Peclet number of $\mathrm{Pe} = 1 \times 10^2$ (solid lines), $\mathrm{Pe} = 1 \times 10^3$ (dashed lines), $\mathrm{Pe} = 1 \times 10^4$ (dotted lines) and $\mathrm{Pe} = 1 \times 10^5$ (dash-dotted lines).

diffusion is used as a model for the effects of hydrodynamic interactions between the disks. We further note that the (near) shear rate $\dot{\gamma}$ invariance of $[\eta]$ (inset in Fig. 2b) indicates a constant rotary Peclet number, i.e. $D_r \sim \dot{\gamma}$.

We now present linear stability analysis of the cylindrical coordinate version of Eqs. (1-4), w.r.t. axisymmetric perturbations $u'(r)\exp(\mathbb{i}kz)\exp(\lambda t)$ where k is the axial wavenumber and λ is the growth rate. The axisymmetry of the instability modes is experimentally observed in Figs. 3a-b. Details of the stability analysis are given in Ref. [8]. Briefly, we discretise Eqs. (1-4) using the Chebyshev collocation method on 30 collocation points. After computing the base state, we compute λ by numerically solving the corresponding generalised eigenvalue problem. All λ are found to be real-valued, i.e. non-oscillatory, in agreement with the experimental observations in Figs. 3a-b.

To match the experimental system, we use a radius ratio of $R_1/R_2 = 0.77$, a disk aspect ratio of $r_a^{-1} = 10^2$ and we vary the disk concentration between $c = 10^{-4}$ and $c = 10^{-1}$ and the rotary Peclet number between $\mathrm{Pe} = 10^2$ and $\mathrm{Pe} = 10^5$. For each c and Pe we vary the wavenumber k of the perturbation and for each k we vary the rotation speed Ω. We thereby find the critical wavenumber k_c and the critical Taylor number Ta_c that mark the transition between positive and negative λ, i.e. the onset of instability.

Fig. 4 shows good qualitative agreement between the computed and measured Ta_c and k_c as functions of c. The experimentally measured k_c show a slight discontinuity between $c = 10^{-2}$ and $c = 2 \times 10^{-2}$ which is likely due to the change in the suspending medium (see experimental section) and the corresponding changes in sedimentation and inter-particle adhesion. These effects are considered weak, however, since the measured Ta_c (Fig. 4) does not show a discontinuity. The experimental data for Ta_c agree well with the numerical results for $10^3 \lesssim \mathrm{Pe} \lesssim 10^4$. This range is beyond the value of $\mathrm{Pe} \approx 22$, that was required to match the constitutive model to experiments for steady shear flow (Fig. 2b). This discrepancy highlights that rotary diffusion is not an accurate model for hydrodynamic interactions between disks. This seems consistent with the notion that in addition to a randomising effect, interactions between disks may also have the opposite effect of suppressing rotation due to geometrical constraints [29]. Nevertheless there is good qualitative agreement between the theory and the experimental data, in both Ta_c and k_c as functions of c. This agreement supports the finding of a new Taylor Couette instability that is driven by anisotropic viscous stresses in suspensions of disks.

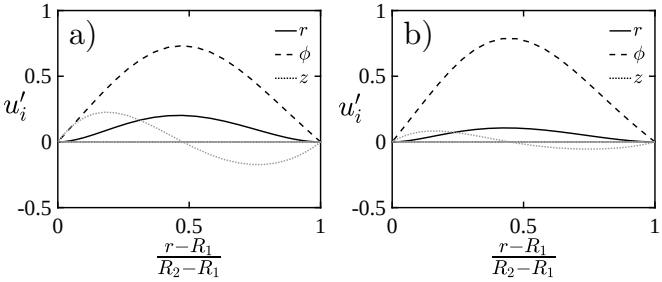

FIG. 5: Real part (black) and imaginary part (grey) of computed instability mode in a Newtonian system (a) and in a disk suspension (b), using an aspect ratio of $r_a^{-1} = 10^2$, a rotary Peclet number of $\mathrm{Pe} = 3 \times 10^3$ and a concentration of $c = 10^{-2}$.

Fig. 5 shows the computed velocity profiles for the Newtonian mode with $c = 0$ and $\mathrm{Ta} = \mathrm{Ta}_c \approx 48$ and for the disk mode with $c = 10^{-2}$ and $\mathrm{Ta} = \mathrm{Ta}_c \approx 24$. Compared to the Newtonian mode, the disk mode has a suppressed cross stream velocity. These results agree qualitatively with the intensity maps in Figs. 3a-b, showing that the Newtonian mode has a relatively large intensity immediately at $\mathrm{Ta} = \mathrm{Ta}_c$ which stays roughly constant for $\mathrm{Ta} > \mathrm{Ta}_c$, whereas the disk mode has a relatively small intensity at $\mathrm{Ta} = \mathrm{Ta}_c$ which increases for $\mathrm{Ta} > \mathrm{Ta}_c$.

Summarising, we have provided experimental evidence for a new type of Taylor Couette instability that is driven by neither centrifugal forces nor by fluid elasticity. Instead it is driven by anisotropic viscous forces in suspensions of disks that redirect the transfer of azimuthal momentum from the radial to the axial direction. The instability is qualitatively well described by constitutive equations of dilute spheroid suspensions. Quantitative differences between the theory and the experiments are most likely due to hydrodynamic interactions between the disks, and we expose the limitations of rotary diffusion as a model to quantitatively account for these effects. This new hydrodynamic instability has a range of potential industrial applications, e.g. to enhance mixing in

chemical reactors or to enhance heat transfer in drilling equipment. The instability may also be important when interpreting Taylor Couette rheometer measurements.

[1] G. I. Taylor, Phil. Trans. R. Soc. Lond. Ser. A **223**, 289 (1923).
[2] T. J. Lockett, S. M. Richardson, and W. J. Worraker, J. Non-Newtonian Fluid Mech. **43**, 165 (1992).
[3] B. Alibenyahia, C. Lemaitre, C. Nouar, and N. Ait-Messaoudene, J. Non-Newtonian Fluid Mech. **183**, 37 (2012).
[4] N. Cagney and S. Balabani, Phys. Fluids **31**, 053102 (2019).
[5] V. Sinevic, R. Kuboi, and A. Nienow, Chem. Eng. Sci. **41**, 2915 (1986).
[6] M.-K. Yi and C. Kim, J. Non-Newtonian Fluid Mech. **72**, 113 (1997).
[7] V. K. Gupta, R. Sureshkumar, B. Khomami, and J. Azaiez, Phys. Fluids **14**, 1958 (2002).
[8] J. Gillissen and H. Wilson, Physical Review Fluids **3**, 113903 (2018).
[9] M. V. Majji and J. F. Morris, Phys. Fluids **30**, 033303 (2018).
[10] P. Ramesh, S. Bharadwaj, and M. Alam, J. Fluid Mech. **870**, 901 (2019).
[11] J. Gillissen and H. Wilson, Physical Review Fluids **4**, 043301 (2019).
[12] M. E. Ali, D. Mitra, J. A. Schwille, and R. M. Lueptow, Phys. Fluids **14**, 1236 (2002).
[13] R. H. Thomas and K. Walters, J. Fluid Mech. **18**, 33 (1964).
[14] R. G. Larson, E. S. G. Shaqfeh, and S. J. Muller, J. Fluid Mech. **218**, 573 (1990).
[15] A. Groisman and V. Steinberg, Phys. Ref. Lett. **77**, 1480 (1996).
[16] M.-A. Fardin, D. Lopez, J. Croso, G. Grégoire, O. Cardoso, G. McKinley, and S. Lerouge, Physical review letters **104**, 178303 (2010).
[17] N. Liu and B. Khomami, J. Fluid Mech. **737** (2013).
[18] A. M. Philippe, C. Baravian, M. Jenny, F. Meneau, and L. J. Michot, Phys. Rev. Lett. **108**, 254501 (2012).
[19] C. Baravian, D. Vantelon, and F. Thomas, Langmuir **19**, 8109 (2003).
[20] C. S. Dutcher and S. J. Muller, J. Fluid Mech. **641**, 85 (2009).
[21] R. DiPrima, P. Eagles, and B. Ng, Phys. Fluids **27**, 2403 (1984).
[22] G. S. Beavers and D. D. Joseph, Phys. Fluids **17**, 650 (1974).
[23] H. Brenner, Int. J. Multiphase Flow **1**, 195 (1974).
[24] F. Folgar and C. L. Tucker III, J. Reinf. Plast. Compos. **3**, 98 (1984).
[25] E. S. Shaqfeh and G. H. Fredrickson, Phys. Fluids **2**, 7 (1990).
[26] D. L. Koch, Phys. Fluids **7**, 2086 (1995).
[27] C. A. Stover, D. L. Koch, and C. Cohen, J.Fluid Mech. **238**, 277 (1992).
[28] M. Rahnama, D. L. Koch, and E. S. Shaqfeh, Phys. Fluids **7**, 487 (1995).
[29] A. B. D. Brown, S. M. Clarke, P. Convert, and A. R. Rennie, J. Rheol. **44**, 221 (2000).